Materials Research. 2018; 21(2): e20170911
DOI: http://dx.doi.org/10.1590/1980-5373-MR-2017-0911

Mechanical and Metallurgical Characterization of Laser Welding on P91 Ferritic Steel and Incoloy 800HT Dissimilar Joints

Lakshmanan Vellaichamy[a], Pradeep Benedict Thomas Gerard[a], Sathiya Paulraj[a]*

[a]Department of Production Engineering, National Institute of Technology, Tiruchirappall, 620015, Tamilnadu, India

Received: October 06, 2017; Revised: November 30, 2017; Accepted: December 30, 2017

In this work, microstructural characterization and mechanical properties of P91 and Incoloy 800HT dissimilar laser beam welded joint were analyzed. In addition to that, metallographical studies were conducted using Optical microscopy, Scanning electron microscopy (SEM) equipped with Energy-dispersive X-ray spectroscopy (EDX) and X-Ray diffraction analysis (XRD). Effect of specific point energy on weld microstructure was predicted and it was compared with fusion zone hardness. The δ-ferrite content of the welds was predicted and it was correlated with the results measured by ferritoscope. Increase in heat input led to a minimal increase in the weld bead width and also the depth of penetration as predicted by microstructural studies. The traces of δ-ferrite in the interface of P91 side led to higher strength and microhardness of the weld. Failure of tensile specimens in the HAZ of Incoloy 800HT side was because of lower ferrite content (0 to 0.36) in that region and also due to the presence of the brittle intermetallic phases. The tensile strength of higher specific point energy welds was greater compared to other welds because of precipitation hardening and presence of δ-ferrite. Fractography results of fracture surfaces contain uniform dimples which showed that the failure took place in a ductile mode.

Keywords: *Yb: YAG laser welding, Incoloy 800HT, P91, δ-ferrite, Tensile strength, microhardness.*

1. Introduction

Power production industries aim at higher power production capacity by increasing the pressure and temperature inside the boilers. Hence, there is the need for developing new materials to withstand higher temperatures and pressures. They are being continuously developed in order to meet out the requirements of power production industries. Of the various materials used in power plants, P91 is one of the widely preferred materials in fabrication of boiler components as it has a very good creep strength and high resistance for stress corrosion cracking. P91 is mostly used in the locations of low temperatures, whereas in the regions of high temperature 800 alloys are generally preferred as they have very good strength and oxidation resistance even at higher temperatures. In addition to that, 800 alloys also have an excellent resistance for carburization and a very good corrosion resistance at elevated temperatures. In order to balance the quality of the weld with the economic aspects, fabrication of boiler components are done by joining dissimilar metals. Dissimilar joints are made in such a way that, at higher temperature locations 800 alloys are used and in low temperature locations, alloys like P91 are used as they are comparatively cheaper than the 800 alloys. Gas Tungsten Arc Welding (GTAW) process is generally used for joining these dissimilar metals and in order to have quality joints between P91 and 800 alloys, the major challenges that have to be overcome are the thermal cyclic stresses occurring due to the difference in thermal expansion co-efficient of the materials, reduction in the carbon content in the base metal areas as they migrate towards the weldments, and the formation of oxide notches in the interface of the P91 side due to the stress oxidation. In order to overcome these challenges in most of the works related to GTAW welding of P91 and 800 alloys, nickel based filler materials are used as the diffusivity of carbon in nickel alloys are less[1]. In some cases, the welds obtained using the nickel filler materials resulted in the formation of cracks along the interface of P91 side. Madhusudhan Reddy et al.[2] conducted studies on the effect of different welding methods on mechanical properties and microstructural features of dissimilar ferritic-austenitic stainless steel weldments. They observed that the residual stress and hardness values were comparatively more on the ferritic stainless steel side, which in turn affected the overall strength of weld. Sayiram et al.[3] studied the microstructural aspects of dissimilar joints between Incoloy 800H and 321 austenitic Stainless Steel using GTAW welding process. They observed a competitive growth mechanism in the interface of the Incoloy 800H side. The existing welding techniques like Gas Tungsten Arc Welding (GTAW) require preheating and inter-pass heating during welding. So the joints produced more distortion and Inter-critical softening was observed in GTAW welding. To overcome the disadvantages of GTAW, laser beam welding is suggested to improve the quality. Laser has become inevitable in welding industries as it has the have

*e-mail: psathiya@nitt.edu

capability to produce weld with lesser heat affected zone, lesser distortion and it has successfully used for joining wide variety of similar, dissimilar materials. Improvement in the quality of the weld is mainly due to the fiber laser which involves less capital investment[4]. And also laser welding shows lesser quantity of laves phase weld microstructure with lower Nb concentration which is advantageous over the GTAW welding process[5]. Shanmugarajan et al.[6] studied the metallurgical properties of autogenous laser welded P92 material. They had performed macrostructure analysis to measure bead width and depth of penetration and concluded that with an increase in laser power, depths of penetration of the welds get increased. Generally in dissimilar welding processes, the filler metal composition and crystal structures are different from the base metals which in turn results in non-epitaxial growth and new grains will be nucleating at the weld fusion boundary[7]. The weld metal morphology in dissimilar joining was mostly cellular and dendritic influenced by the chemical composition, temperature gradient and solidification speed[8]. Cleiton Silva et al.[9] evaluated dissimilar welds between ferritic and austenitic steels and concluded that the fusion zone microstructure has a characteristic δ-ferrite acicular morphology, from which the amount of δ-ferrite got changed with the increase in heat input. The solidification morphology studies revealed that Inconel 600 and AISI 304 joints must be cellular-dendritic and the HAZ needs to be totally austenitic[10,11]. Schneider et al.[12] accomplished a substantial improvement of process stability by optimizing the shielding gas flow rate for suppressing the vapor plume. Bhaduri et al.[13] conducted experiments on Incoloy 800 to 9Cr-1Mo dissimilar welding and suggested that the effect of aging on the tensile properties was very less. Several results had stated that solidification cracking was reduced by keeping a considerable amount of delta ferrite (3-10%) in the weld, which efficiently reduced the grain growth and increased the mechanical properties[14,15]. In most of the works related to laser welding processes, Nd: YAG fibres are used and only a very few works have been done using Yb: YAG fiber which has comparatively lesser wavelength than the Nd: YAG lasers. Lesser wavelength of laser will help in increasing the absorption. Deepan Bharathi kannan et al[16] successfully used Yb: YAG fiber laser for joining NiTinol shape memory alloys.

Through literatures it is understood that, no work has been are done related to joining of P91 and Incoloy 800 HT alloys. With the development of next series in 800 alloys called Incoloy 800 HT, it has further widened the possibility of increasing the temperatures and pressures inside the boilers as they have better properties at higher temperatures than 800 alloys. General problems associated with GTAW welding are the interpass temperature required, number of passes required to attain full penetration, preheat temperatures and the selection of correct filler material. Hence, the alternate option will be the other welding processes like laser welding which has the capability to weld thick plates even in a single pass and results in lesser heat affected zone. Hence in this work for the first time an attempt is made to join P91 and Incoloy 800 HT steels using Yb: YAG laser welding process. Shielding gas with the help of two nozzles was initiated in our research which is not so far carried out in these materials. The essence of this study comes with the feasibility of the dissimilar weld and also the analysis of the mechanical properties and Microstructural characterization. Which are in turn useful for the power plants and some high temperature applications.

2. Materials and Methods

The materials selected for these studies are Incoloy 800HT and P91. Chemistry of the base materials were analyzed using spectroscopy method and the same is given in Table 1.

The dimensions of the plates were 200 mm*150mm*4 mm and laser butt welding experiments were carried out using power capacity of 4kW 6-Axis KUKA robot Yb: YAG laser welding solid state laser (focal spot size was maintain at 0.2mm, wavelength:1030nm, Beam diameter: 0.22mm as constant). Laser welding input parameters are given in Table 2. Three experiments runs were conducted by varying laser power in three different ranges keeping the welding speed at a constant value. Through trial and error methods, we have identified the following parameters

$$\text{Heat Input} = \text{laser power}/\text{welding speed} \quad (1)$$

$$\text{Specific Point Energy} = (P \times D)/V \quad (2)$$

Where the laser powers (P), laser beam diameter (D), welding speed (V) respectively.

It is understood that with an increase in laser power, there is a steady increase in the heat input to the weld which in turn increased the volume of the metal melted. A trend in increase in tensile strength was observed with an increase in laser power. Ytterbium Continuous wave (YCW) mode fiber laser welding of 4 mm thick dissimilar plates was investigated. The general schematic of laser welding is presented in Figure 1.

To avoid fusion zone contamination, argon (Ar) was used as a shielding gas with a constant flow rate of 14 lpm. After welding, the samples were cut using the abrasive cutting machine in the required dimensions and conventionally arranged for metallographic analysis. The cross sections of the weld were polished using 300,600, 800,1000, 1200 grades emery sheets of SiC followed by fine polishing by automatic polishing machine with 5µm alumina powder and an air blower was used to dry the specimen.

After polishing, electrolytic etching was done in two solutions namely 10g, of CrO_3 +100ml distilled followed by

Table 1. The chemical composition of the base material (wt-%):

	C	S	N	Cr	Ni	Mn	Si	Ti	Cu	P	Al	Co	Mo	Nb	V	Fe
INCOLOY 800HT	0.06	0.002	0.013	20.63	30.56	0.69	0.46	0.34	0.10	0.008	0.87	0.08	-	0.01	-	46.17
P91	0.11	0.0038	-	9.46	0.09	0.46	0.31	-	-	0.015	-	-	0.88	0.06	0.20	Bal

Table 2. Laser welding input parameter

	Laser Power (kW)	Welding Speed (m/min)	Heat Input (KJ/cm)	Specific pointenergy (J)
Experiment 1	2.4	1	1.40	32.18
Experiment 2	2.5	1	1.50	33.50
Experiment 3	2.6	1	1.56	34.87

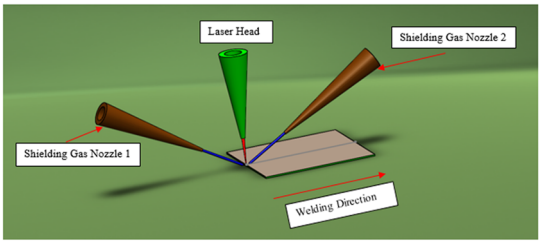

Figure 1. Schematic of Laser welding

Villella's reagent solution 1g, of $C_6H_3N_3O_{7+}$ 5ml of HCL + 100ml of C_2H_6O. Macrostructures of the weldments were taken using Welding Expert System software (Struers, Austria) with the magnification range of 20X. Moreover, microstructures were analyzed using the optical microscopy (Make: SuXma series MET-UI). X-ray diffraction (XRD) was performed to confirm the phases present in the base metalsand weld metals. Fisher ferritoscope (Fisher SMP30) was used to measure the δ-ferrite content in the welds. Elemental composition of the welds was measured by Scanning electron microscope (Make: ZEISS EV018) equipped with Energy dispersive spectroscopy (EDS). Microhardness values of various zones were assessed based on the standard ASTM E384 using Vickers microhardness tester (Make: Wilson Hardness 402 MVD). Microhardness values were measured by applying a load of 500 g for a dwell period of 10 sec. The welded plates were cut according to the ASTM E8/E8M standard with a gauge length of about 50 mm using wire cut electric discharge machine(W-EDM) for tensile tests and the tests were carried out using the Universal testing machine (MAKE-Tinius Olsen) .The ultimate tensile strength and elongation (%) were determined. To understand the fracture modes, fractography analyses were also done by using scanning electron microscope (Make: ZEISS EV018).

3. Results and Discussion

3.1 Macrostructures of the weld

Macrostructures of the welds zone are shown in Figure 2(a-c).

Dye penetrant test and X-ray radiography were done for the welded plates. The results revealed that for except porosity defect for experiment 1 other welds did not reveal any surface or hidden defects indicating that welds were undamaged and were of good quality.

The measured bead geometry values are presented in Table 3. From the Tabulated values it is clear that the increase in laser power leads to increase in the bead width with very minimal difference. The bead geometry (bead width, depth of penetration) of the laser welding depends on rate heat input, power intensity and physical properties

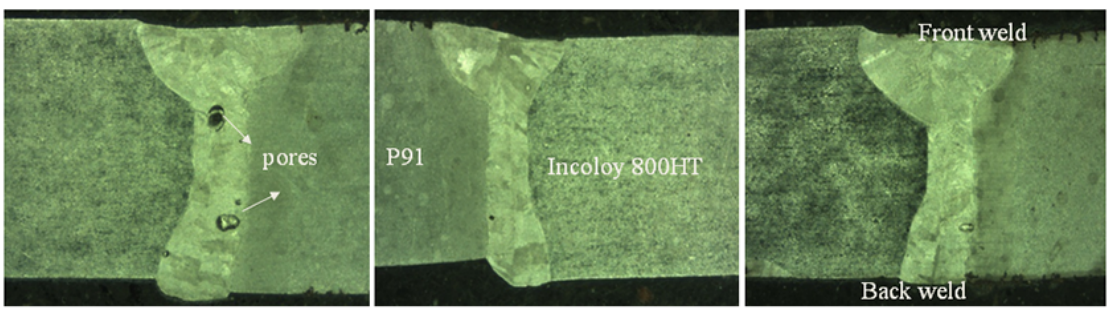

Figure 2. Macrostructures of three different weld zone. (a)Experiment 1(b) Experiment 2 (c) Experiment 3

Table 3. Measured bead geometry values.

	Topbead width (mm)	Middle bead width (mm)	Bottom bead width (mm)	Depth of Penetration (mm)
Experiment 1	2.700	0.901	1.264	4.125
Experiment 2	2.750	0.903	1.273	4.128
Experiment 3	2.925	0.916	1.505	4.135

of the material. Beat geometry analysis also indicates that the materials were sensitive to laser power and any small variation in laser power will have an impact on the geometric parameters of the formed weld bead. From Table 3, it is clear that the marginal increase in the depth of penetration is due to increasing the Laser Power and by increasing the Laser Power, heat input also increases in the laser welding process. Also the heat input is inversely proportional to the cooling rate hence if higher cooling rate prevails in weld, fine grains are formed and also coarser grains are formed in increasing laser power with same welding speed.

Macrostructures of welds with the welded parameters had shown good fusion for all experiments and in experiment 2 and 3 the macrostructures appeared without any defects but in experiment 1, porosities can be seen. The samples welded under insufficient arc shielding gas had the greatest possibility for porosity[17].

In laser welding, transformation energy through keyhole mechanism was used, which resulted in maximum material melting. In this work, weld beads of all three experiments showed full penetration and the weld beads were of keyhole shape. The formation of porosity was directly related to keyhole fluctuation. During welding, the depth and shape of the keyhole got varied and bubble might be produced at the bottom of the liquid melt pool. The bubbles stopped in solidified metal, so it results in the formation of keyhole induced porosity. The distribution of the pores was not even throughout the weld and also the shape was spherical as well as irregular. Weld porosities are a direct function of the laser power and welding speed. The porosity diameter increased at constant heat input. Porosity defects were seen in experiment 1, and this was due to key hole instability and high beam power in laser welding[18].

3.2 Microstructures of base materials

3.2.1 Microstructure in base metal incoloy 800HT

The microstructure, SEM and EDS analysis of the as received base material Incoloy 800HT, are shown in Figure 3. The Incoloy 800HT has equiaxed grains of austenite with infrequent twinning. It consists of microstructure with solid solu tion matrix in which some grains are outlined by the precipitate particles at the boundaries and by twining lines which are shown in Figure 3(a).

As shown in Figure 3(b) titanium carbide (TiC) and titanium carbonitride (TiN) were formed during high temperature exposure due to 0.36% titanium and 0.09% carbon in the Incoloy 800HT[19].The grain structure indicates substantial prolonged deformed grains of austenite, some of which were encompassed by fine grains formed by dynamic recrystallization. It can be cleary seen that TiN and TiC do not dissolve easily during solution annealing even if high soaking temperature are employed[3]. The major elements present in Incoloy 800HT are Fe,Ni,Cr that are observed from EDS analysis as shown in Fig .3(c). The average grain size found by the mean intercept method is about coarser ASTM 5 (grain size-64 μm).

3.2.2 The microstructure of P91 base metal

The microstructure, SEM and EDS analysis of the as received base material P91, are shown in Figure 4

The microstructure of P91 consisted of tempered lath martensitic structures, as shown in Figure 4(b), with expressed grain boundaries Figure 4(a). The P91 high alloy steel was strengthened by using precipitation hardening in addition to solution hardening, dislocation hardening, and boundary or sub-boundary hardening mechanism. In P91, grain boundaries were present in two different types: carbonitrides and intermetallic.$M_{23}C_6$, MX, M_6C, M_7C_3 type carbides were present when the predominantly available metal was found to be chromium (Cr), and where M is Cr, Mo, Nb, V type metallic elements and X is the Carbon and nitrogen atoms. $M_{23}C_6$ precipitates volume percentage was almost 2% and rod shaped and MX precipitates was close to 0.2% and the shape was spherical. In P91 base metal, the major elements are Fe and Cr and it was confirmed by EDS analysis as shown in Figure 4(c). The average grain size found by mean intercept method is about 22 μm as per ASTM No 8 method.

3.3 The microstructure of fusion zone

In experiment 1, weld metal microstructure solidification changed from cellular to fine equiaxed dendritic because of low heat input which resulted from the higher cooling rate and therefore a finer microstructure. In the weld metal region austenitic-ferritic (AF)/ferritic-austenitic (FA) modes of solidification occurred and it is clearly seen in Figure 5(a).

A dissimilar joint was obtained and it demonstrated an inhomogeneous microstructure containing a blend of ferrite and austenite hardening structures in differing degrees because of an incomplete mix of the liquid metals on both sides in the weld. During solidification of weld pool thermal

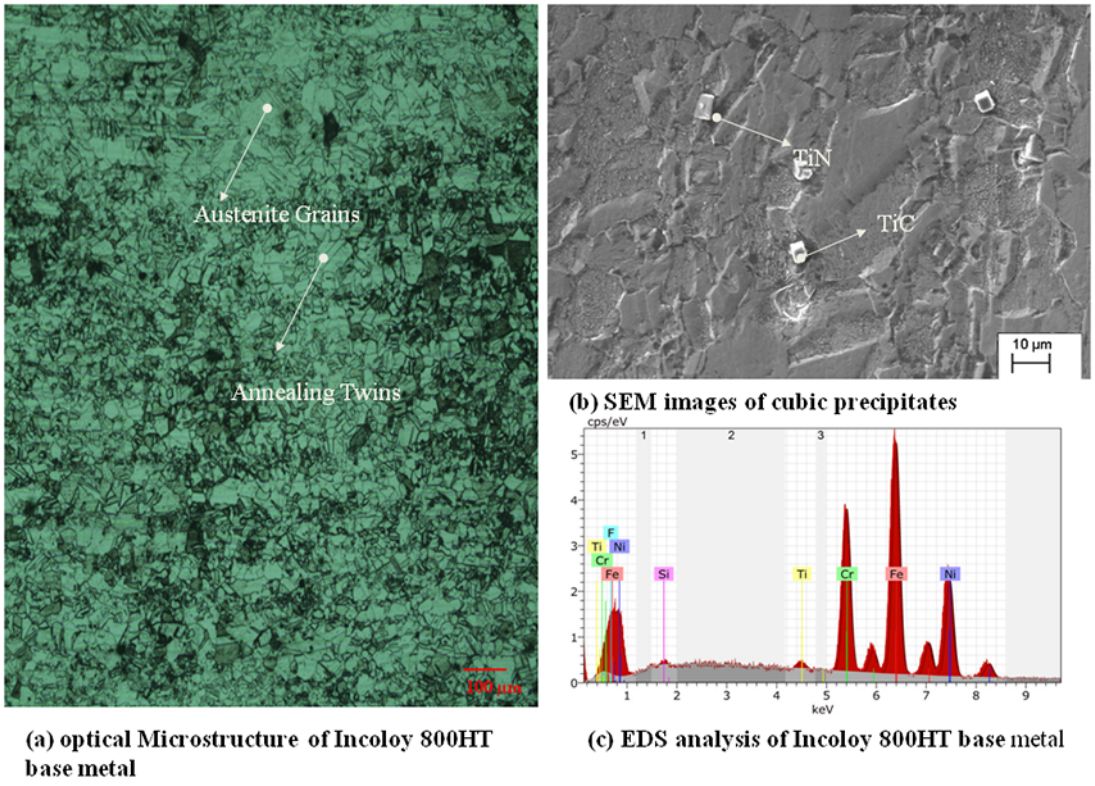

Figure 3. Microstructure, SEM and EDS analysis of the as received base material Incoloy 800HT (a) optical Microstructure of Incoloy 800HT base metal (b) SEM images of cubic precipitates (c) EDS analysis of Incoloy 800HT base metal

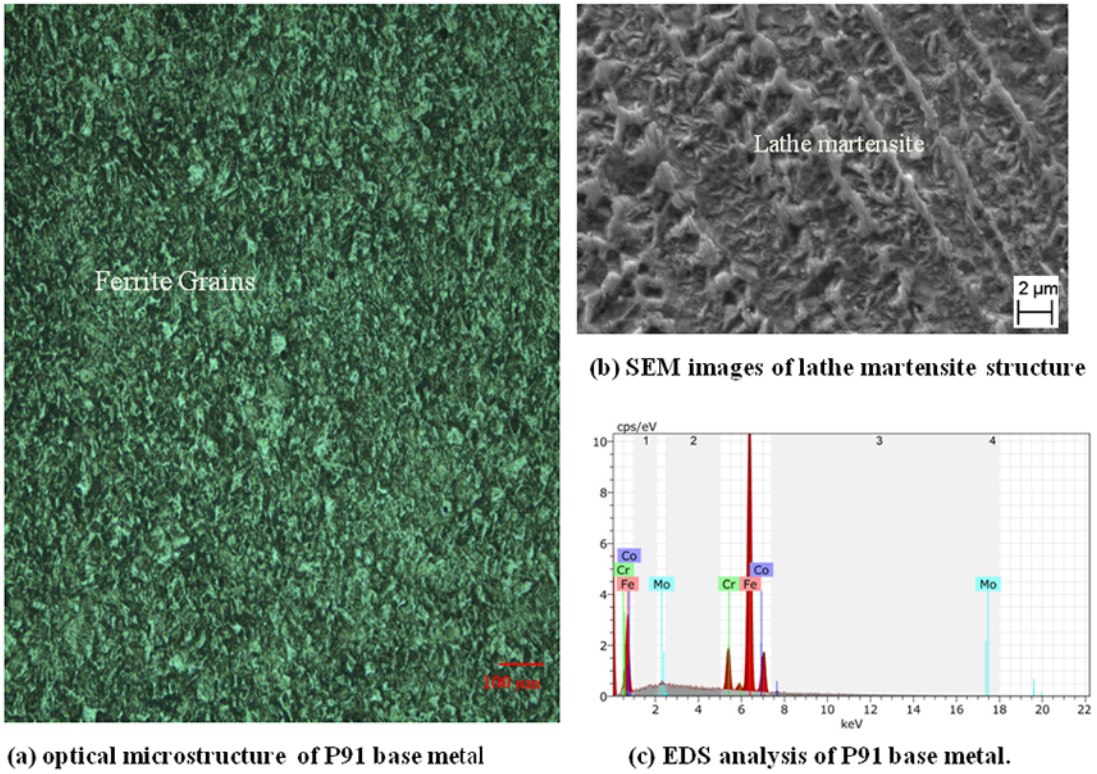

Figure 4. Microstructure, SEM and EDS analysis of the as received base material P91 (a) optical microstructure of P91 base metal (b) SEM images of lathe martensite structure (c) EDS analysis of P91 base metal

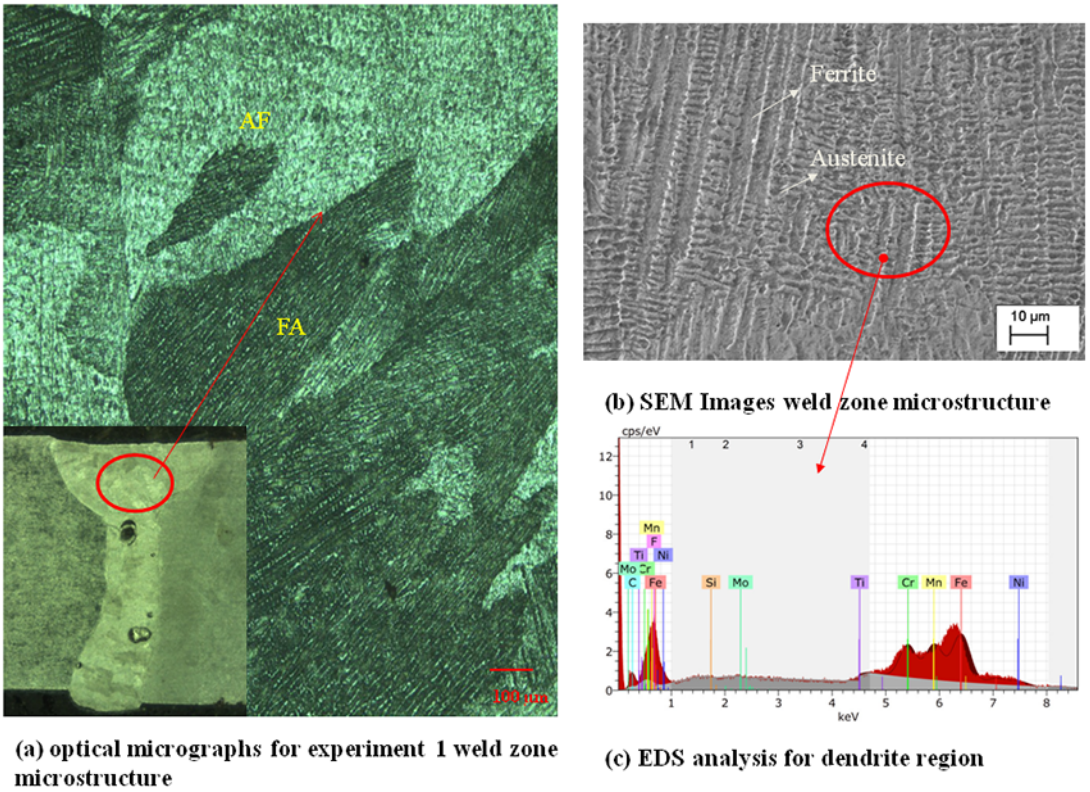

Figure 5. Microstructure, SEM and EDS analysis of the experiment 1 (a) optical micrographs for experiment 1 weld zone microstructure (b) SEM Images weld zone microstructure (c) EDS analysis for dendrite region

contraction stresses are developed that are sufficient enough to break the dendrite arms creating sufficient nucleation sites to develop cellular structure. If the thermal stresses are high enough cellular structure is developed in the weld pool otherwise dendritic structure prevails in the weld zone and some dendritic growth was observed in the fusion zones as shown in Figure 5(b). EDS analysis of the weld zone illustrated that it possessed major elements: Fe, Cr, Ni, Mn and Si, Mo, Ti, C, F elements were also present in minimum amounts as shown in Figure 5(c). Therefore, chromium, molybdenum, iron, nickel, titanium, silicon can diffuse from the weldmetal to the base metal, so to form a secondary precipitates. But carbon diffused from weld metal to base metal and in the weldmetal presence of Ti, Ni, Cr, and Mo precipitates is confirmed by EDS analysis[20]. The OM, SEM and EDS analyses of the fusion zone of the experiment 2 are shown in Figure 6.

In experiment 2, solidification rate R and temperature gradient G together control the solidification microstructure. As solidification rate increases, the temperature gradient gradually decreases. The ratio G/R controls the solidification mode while the product G * R controls the size of the structure[7]. Owing to higher G/R ratio in fusion line, solidification occurs (cellular) towards the center and hence the dendritic growth occurred in the center of the weld. Due to the steep thermal gradients near the fusion boundary, equiaxed dendrites were visible in the weld interior because of lower G/R ratio as shown in Figure 6(a) and columnar dendrites were also seen as shown in Figure 6(b).

EDS analysis of the weld zone illustrated the presence of major elements: Fe, Cr, Ni, Mn and Si, Mo, Ti, C, F elements were also present in minimum amounts in addition to sulphur as shown in Figure 6(c). Therefore, chromium, molybdenum, iron, nickel, titanium, silicon can diffuse from the weldmetal to the base metal, so to form secondary precipitates. But carbon diffused from weld metal to base metal and in the weldmetal presence of Ti, Ni, Cr, and Mo precipitates is confirmed by EDS analysis[20].

Furthermore, the degree of under cooling was inversely proportional to the G/R ratio. The regions adjacent to fusion boundary had sharper thermal gradients than in weld interior[5]. Dissimilar metal Incoloy 800HT and P91 steel laser beam welds contain finer grains because of rapid cooling rates since δ-γ transformation is a diffusion controlled process and the rapid cooling in the welding does not furnish adequate time to finish the phase transformation, consequently, a huge portion of primary δ-ferrite is retained in weldments[21].

OM, SEM and EDS analyses of the fusion zone in experiment 3 are presented in Figure 7 regarding the laser Power, higher the laser power, coarser was the dendritic

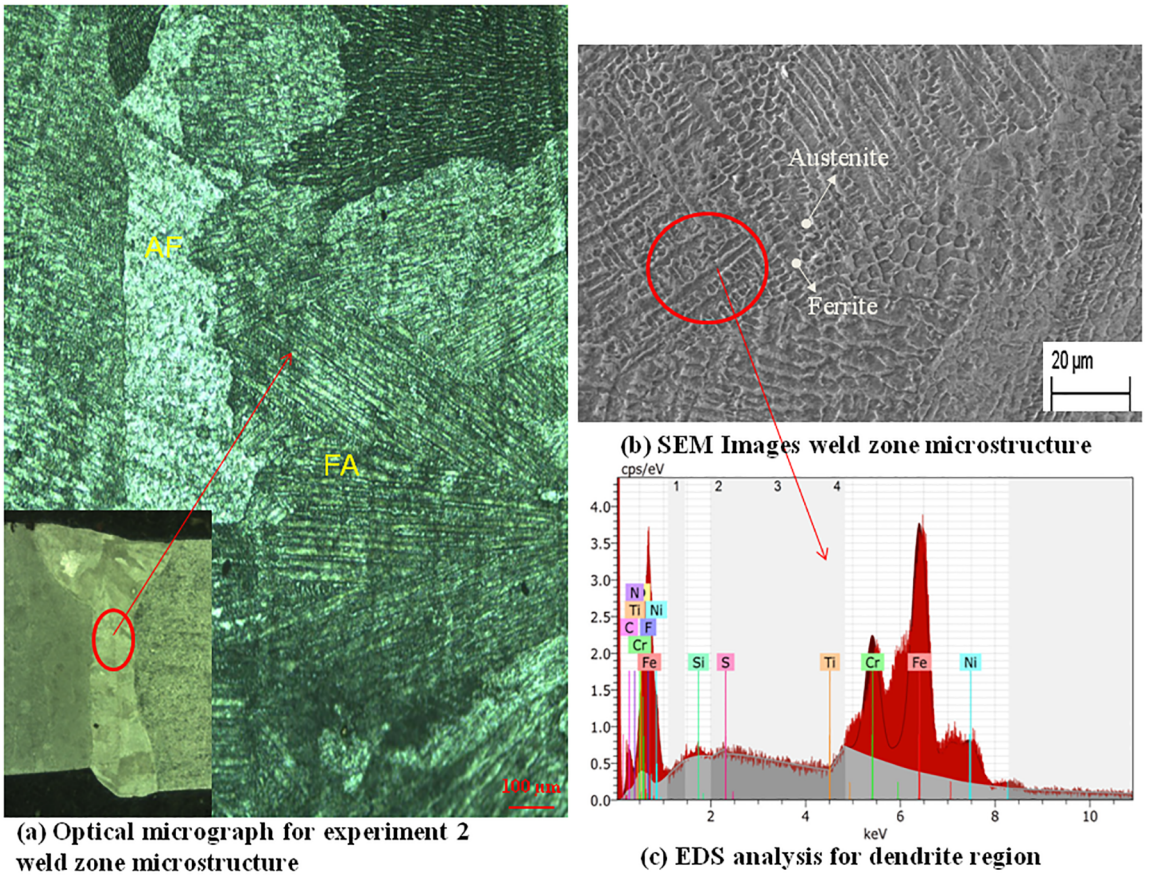

Figure 6. Microstructure, SEM and EDS analysis of the experiment 2 (a) Optical micrograph for experiment 2 weld zone microstructure (b) SEM Images weld zone microstructure (c) EDS analysis for dendrite region

structure because of reduction in cooling rate as shown in Figure 7(a). Although laser power altered the microstructure morphologies, it employed the most significant positive impact on the weld width, weld penetration depth while opposite phenomena were observed for welding speed. Also, because of higher laser power and slower welding speed there existed a higher rate of energy deposition on the weld area. This accounts for fewer variations in the Microstructural aspects for the dissimilar joints obtained.

Metallographic examination using ferritoscope revealed that the ferrite content in these regions were 8.5 to 37.6%. The microstructure of the regions that solidified in the primary austenitic mode was coarser with a limited amount of δ-ferrite which were distinguished in the intercellular boundaries as shown in Fig. 7(b). However, greater amount of vermicular ferrite was seen in the regions that solidified in the FA modes.

Toughness of austenitic stainless steel can be reduced by the presence of ferrite in the microstructure. Addition of Fe in the chemical composition of nickel based alloy will decrease the solubility of Nb in austenite. Equilibrium distribution Nb decreases as the Fe content in the fusion zone increases[22].

Lack of deposited elements like sulphur, Mo and the major elements like Fe,Cr,and Ni are well known for their low tendency to get deposited in the interdendritic and intergranular regions as shown in Fig .7(c). Moreover, the grain size measured for the experiment 2 was about 13 µm whereas in other two experiments it was approximately about 11 µm.

3.4 Microstructure at the interface on the both side

The interface on the weld zone on the P91 side and Incoloy 800HT side are shown in Figure 8(a) & (b). From the optical micrograph analysis it is clear that grain growth occurred from base metal to weld metal and the change in the microstructure of weld zone was analysed. By EDS analysis, the element transfer from the base material to weld metal after welding can be studied.

3.4.1 Microstructure at the interfaces of Incoloy 800HT side

The microstructures at the weld interfaces of Incoloy 800HT side are shown in Fig 9. Weld metal microstructures showed fine equiaxed grains on the Incoloy 800HT side.

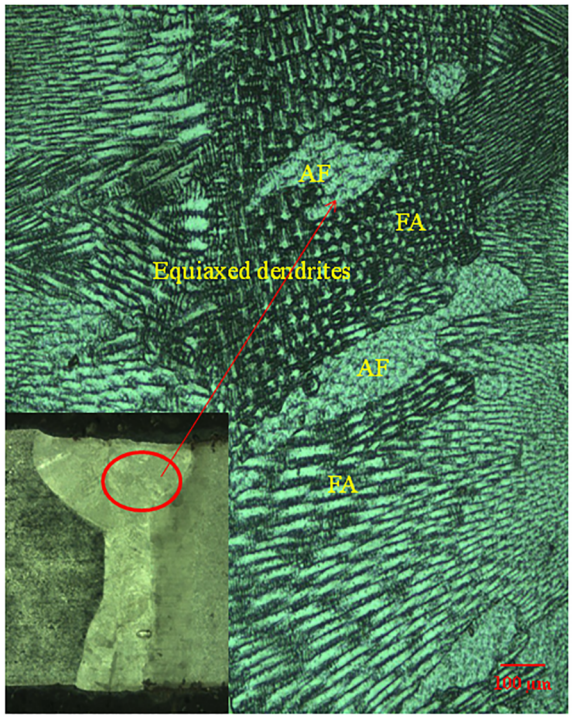

(a) Optical micrographs for experiment 3 weld zone microstructure

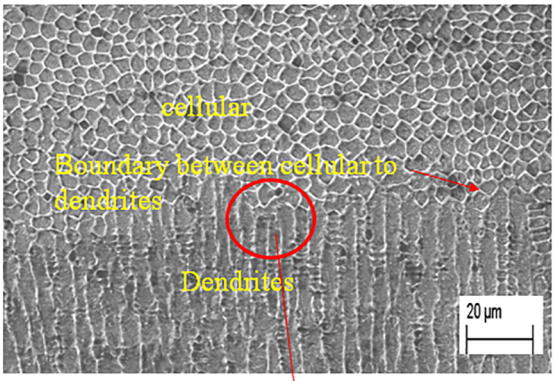

(b) SEM Images weld zone microstructure

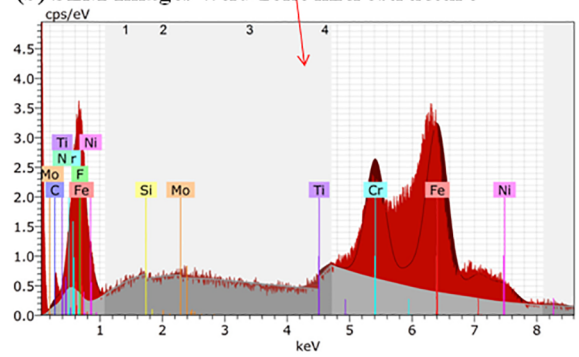

(c) EDS analysis for dendrite region

Figure 7. Microstructure, SEM and EDS analysis of the experiment 3 (a) Optical micrographs for experiment 3 weld zone microstructure (b) SEM Images weld zone microstructure (c) EDS analysis for dendrite region

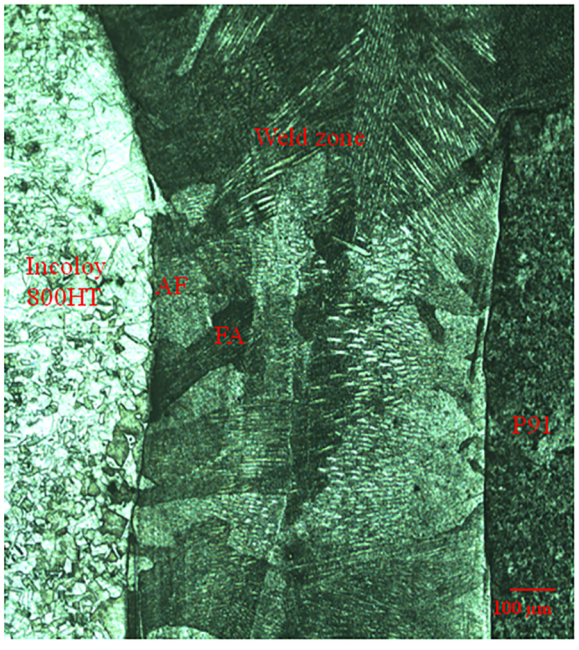

(a) Optical micrograph interfaces between base metal and weld metal middle surface

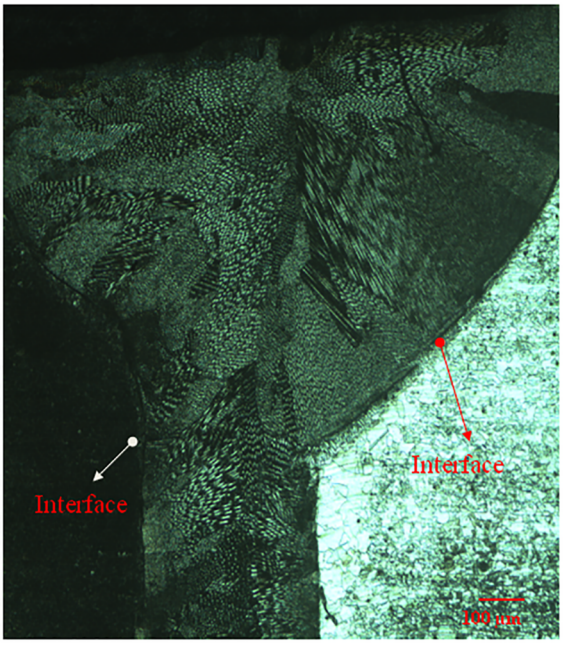

(b) Interfaces between base metal and weld metal top surface

Figure 8. Interface on the weld zone on the P91 side and Incoloy 800HT side (a) optical micrograph interfaces between base metal and weld metal middle surface (b) interfaces between base metal and weld metal top surface

Figure 9(a) shows the Optical microstructures and the subsequent SEM image of HAZ is shown in Figure 9(b). The HAZ on Incoloy 800HT side did not exhibit any allotropic transformation because of fully austenite structure. As observed, the fine equiaxed grain size was about 200-300µm and annealing twins of thickness of about 100µm coexisted in HAZ, and TiN and TiC precipitates were formed after welding in HAZ zone.

The large elongated cellular and dendrites grew perpendicular to the fusion boundary in the epitaxial growth structure. It is important to mention that two types of boundaries namely Type I and Type II were seen. Difference between the type I and type II is that in type I, the boundary is in a direction roughly perpendicular to the fusion boundary caused by epitaxial growth as observed generally in similar base and filler materials. In type II the boundary is in a direction parallel to the fusion boundary, Owing to the allotropic transformation in dissimilar welding during cooling at the fusion boundary, type II boundaries were observed more when compared with type I[20].

The extensive lengthened cell and dendrites developed opposite to the combination limit in the epitaxial development structure. It is intriguing to note two sorts of limits named Type I and Type II. The Type I length was shorter as clearly shown in Figure 9(b).

In the Interface of Incoloy 800HT weld metal side, due to the effect of heat input, grain growth can be seen in the heat affected zone and in the fusion zone. The grains in the fusion zone were perpendicularly grown in the initiation process which is called epitaxial growth[22]. The epitaxial growth is useful to increase the strength and ductility of weld metal.

The major and minor element present in the interface after welding were shown in Figure 9(d). From the EDS elemental analysis it is clear that some of the major element like Fe, Ni, Cr, were transferred from base metal side to weld metal and minor elements such as Ti, S, C, had the possibility to form new precipitates like TiN, TiC, etc. and it was confirmed through XRD analysis. And also higher magnifications in interface dendritic arms between precipitates are presented is clearly seen in Figure 9(c). Consequently, strength and hardness got increased in the fusion zone. In the interface between the weld zone and the Incoloy 800HT austenitic dendrites were formed during solidification, which was accomplished by the high level of Ni in this region that

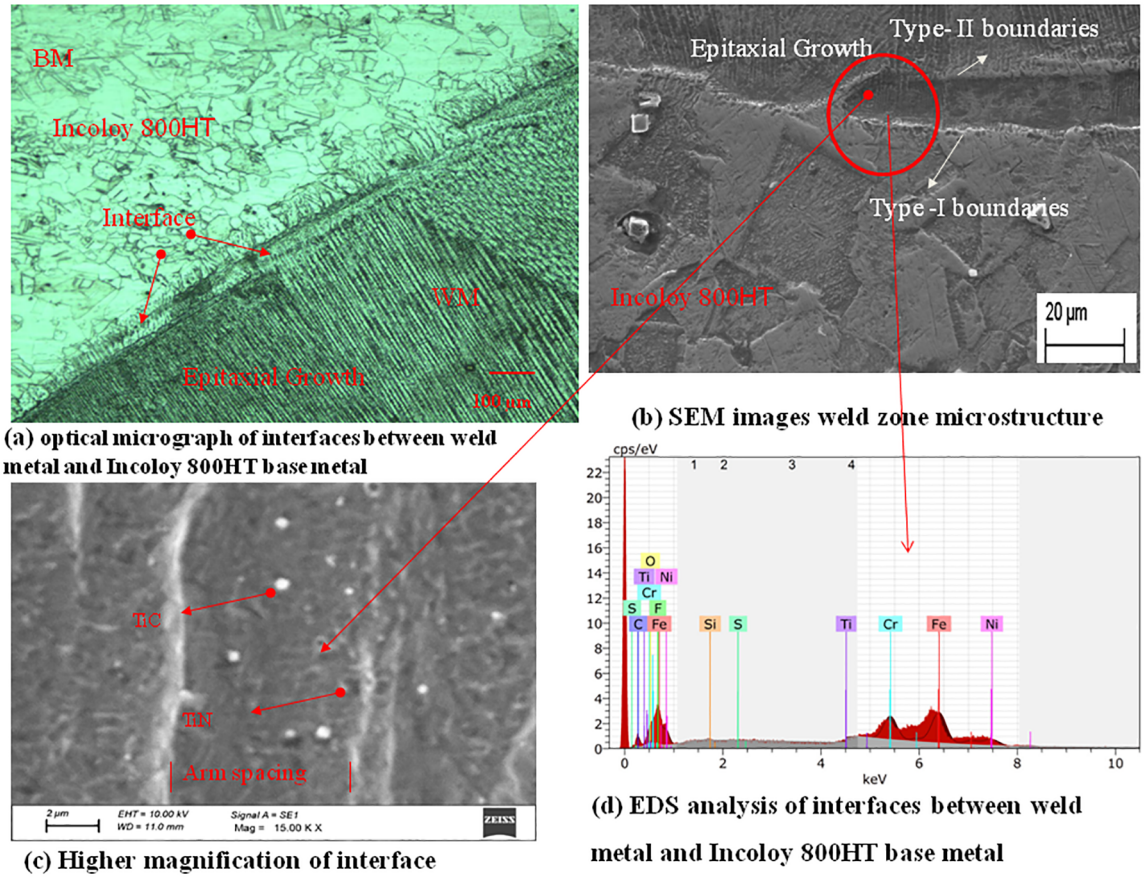

Figure 9. Microstructures at the weld interfaces of Incoloy 800HT side (a) optical micrograph of interfaces between weld metal and Incoloy 800HT base metal (b) SEM images weld zone microstructure (c) Higher magnification of interface (d) EDS analysis of interfaces between weld metal and Incoloy 800HT base metal

was confirmed from the EDS results. Hence, the fusion zone comprised only austenitic phase in the areas close to the Incoloy 800HT interface side[8]. The crystallographic alignment bonding between the δ-ferrite and the austenite governs the ferrite morphology after the post-solidification transformation[7]. It was found that reduction of the impact toughness of the welds was due to increase in the quantity of δ-ferrite in the weldments.

3.4.2 Microstructure at the interfaces of P91 side

The microstructures at the weld interfaces of the P91 side are shown in Fig 10.

It is believed that such a distinction in microstructure at various areas of the welding bead as appeared in Figure 10(a).mainly comes about because of the thermal gradient shift amid welding process. At the point when the welding bead moves, more refined microstructure with cellular morphology was formed because of the rapid heating and cooling at the top of the bead. The dendritic structures were created by reheating and cooling during overlapped weld bead movement. The cooling rate ought to be the principle reason for the change in microstructure from cellular to dendritic

The microstructures in the fusion zone were formed due to solid phase transformation and solidification behaviour, which in turn were controlled by weld cooling rates and chemical compositions. The melting ratio of the two materials to be welded predominantly decides the chemical composition in the fusion zones. The width of the HAZ is high compared to Incoloy 800HT side , because of the fact that the coefficient of thermal expansion (CTE) of austenite being higher than that of ferritic, and the thermal conductivity of austenite being lower than the ferrite and these features result in a higher level of thermally generated stress[23]. The large elongated cellular and dendrites grew perpendicular to the fusion boundary in the epitaxial growth formation as shown in Figure 10(b).

The fusion zone microstructures were formed as an effect of solidification behavior and forthcoming solid-phase transformation, which in turn was governed by cooling rates and chemical composition. Furthermore, the chemical composition in the fusion zone of a dissimilar weldment relies on the welding process parameters. Thus, the fast cooling rates are typical in laser welding which is accountable for the development of very fine dendritic structure in the fusion zone. Also, the average grain size of the weld was about 11 µm (ASTM No- 10). In P91 interface, the weld zone solidified into δ-ferrite, which was recognized by higher levels of Cr and Fe in this region measured by using EDS as shown in Figure 10(c). The results of EDS analysis showed the composition of such phases as mainly Fe, Cr and Ni and the component of Fe may be the few- rich bcc solid solution.

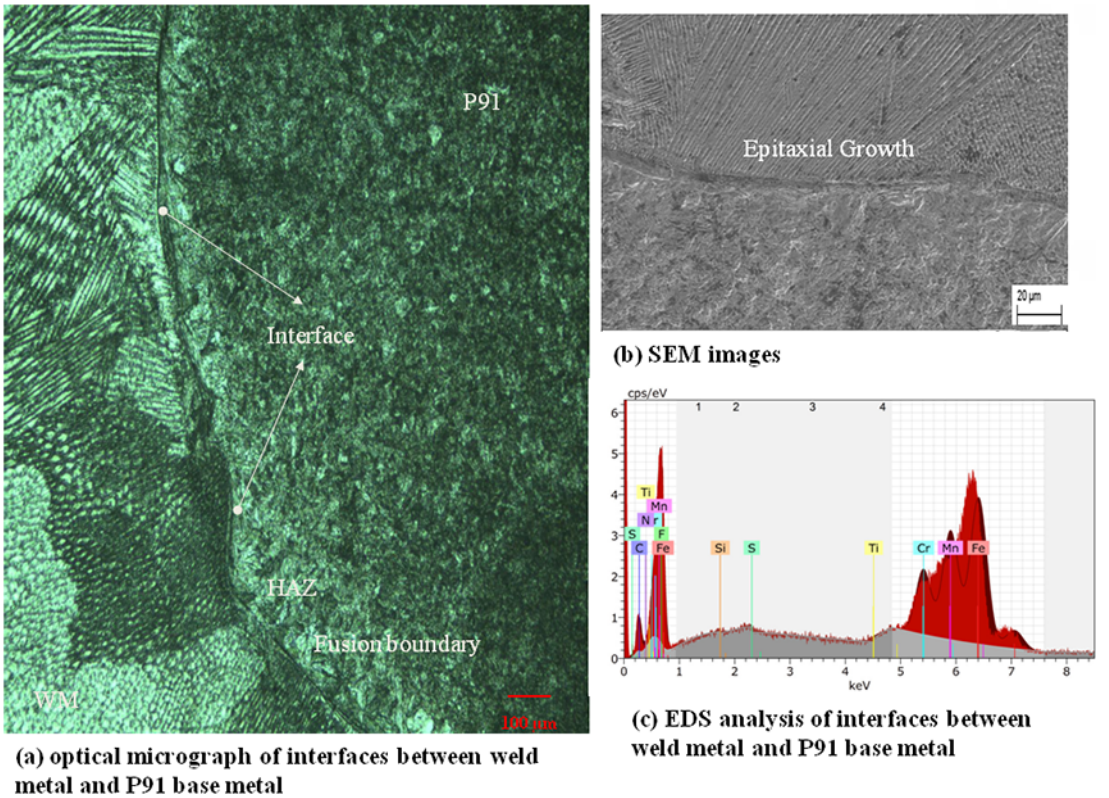

Figure 10. Microstructures at the weld interfaces of P91 side (a) optical micrograph of interfaces between weld metal and P91 base metal (b) SEM images(c) EDS analysis of interfaces between weld metal and P91 base metal

3.5 EDS colour mapping of the weld

The SEM image of Experiment 3 is shown in fig 11(a). The colour mapping of the welds from EDS analysis is shown in Figure 11(b).

The compositional colour mapped images displayed the elemental distributions for the weld. In the elemental compositional maps, bright colours represented the regions of higher concentration elements and slightly dull colour showed the lesser concentration elements. In the weld, elemental distributions of Fe, Cr, Mn were more where distributions of elements like Si ,Ti were less. Moreover, EDX element mapping of Experiment 3 is shown in Fig 12.

The EDS mapping analysis of weld zone shows the different elemental concentration and in the low density elements like (Si, Ti, N,C) intermixing were large as compared with high density (Cr, Ni, Fe) elements. Mn content in the inclusion was higher than that of the matrix. In addition to this, Mn-depleted zone between the matrix and inclusion was seen.

This precipitates results were confirmed by EDS elemental mapping analysis in Figure 12. Same types of results have also been reported by others[20]. It has been reported that titanium nitrides or titanium carbide cannot be dissolved easily during solution annealing even if high soaking temperatures are employed.

3.6 X-Ray diffraction analysis

XRD analysis for both base and weld metal are shown in Figure 13. As observed from the patterns , the intensity of peaks increased based on the specific point of energy and peaks did not shift. However in the weld zone of Incoloy 800HT and P91 joint brittle intermetallic compounds were formed for instance FeNi, $TiFe_2$,TiNi, and Nbc. Formation of these intermetallic compounds effectively reduce the mechanical properties[24].

3.7 Ferrite content

Both Incoloy 800HT and P91 base metals were assumed to be in the equal level of dilution. The ferrite content of this dissimilar weld metal was predicted using WRC 1992 diagram based on Cr and Ni equivalent values and it is shown in Figure 14. The ferrite level was measured to be in the range 2-4 % for the weld metal. The ferrite content was analyzed using ferrites cope (Fischer) as extended ferrite number. In the Incoloy 800HT ferrite content was (0 to 0.25) and P91 parent region ferrite content was of (65 to 77). On the other hand ferrite level range in the fusion zones of experiment 1 was (3 to 25.8), weld zone experiment 2 was (1.7 to 5.1) and experiment 3 was (8.5 to 37.6). In heat affected zone (HAZ) region of Incoloy 800HT side ferrite content was (0 to 0.36) and P91 side ferrite content was (68-76)[25] corroborating the predictions made using WRC 1992 diagram.

The chemical composition of the base materials decides the solidification modes in the stainless steel weldments. Moreover, subsequent to solidification, solid-state transformations from the primary to secondary phase occurs[26] and as a result, a combination of both austenite and ferrite is formed. From the WRC 1992 diagram in which Cr_{eq} and Ni_{eq} were plotted in the abscissa and ordinates respectively as shown in Figure 14, the solidification modes and δ-ferrite contents (ferrite no. FN) of the welds were predicted. In the fusion zone as the ratio was relatively high and also with lower welding speeds the solidification mode was first fully ferritic and then shifted to Ferritic-Austenitic FA mode[20].

3.8 Microhardness

The microhardness values across the welds were plotted in the graph as shown in Figure 15. It is illustrious that on the P91 Steel side, the hardness of the HAZ was markedly higher than the other areas in the weldments; however, on

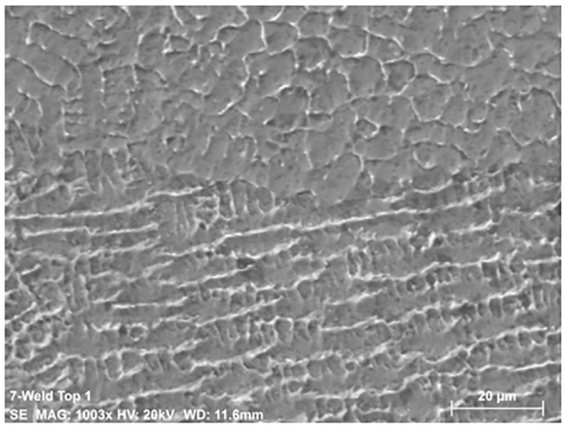

(a) SEM Image of experiment 3

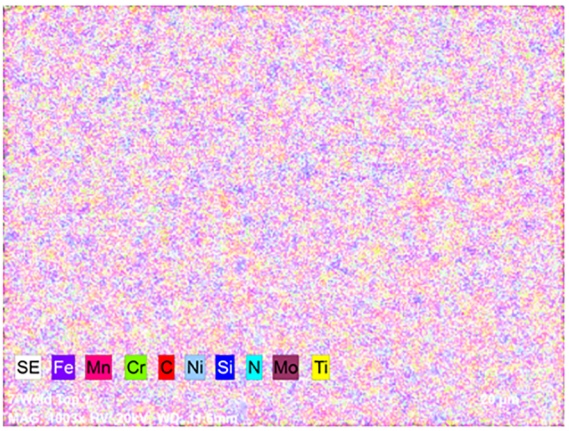

(b) EDS colour mapping of experiment 3

Figure 11. EDS Colour mapping of the weldmetal (a) SEM Image of Experiment 3 (b) EDS colour mapping of Experiment 3

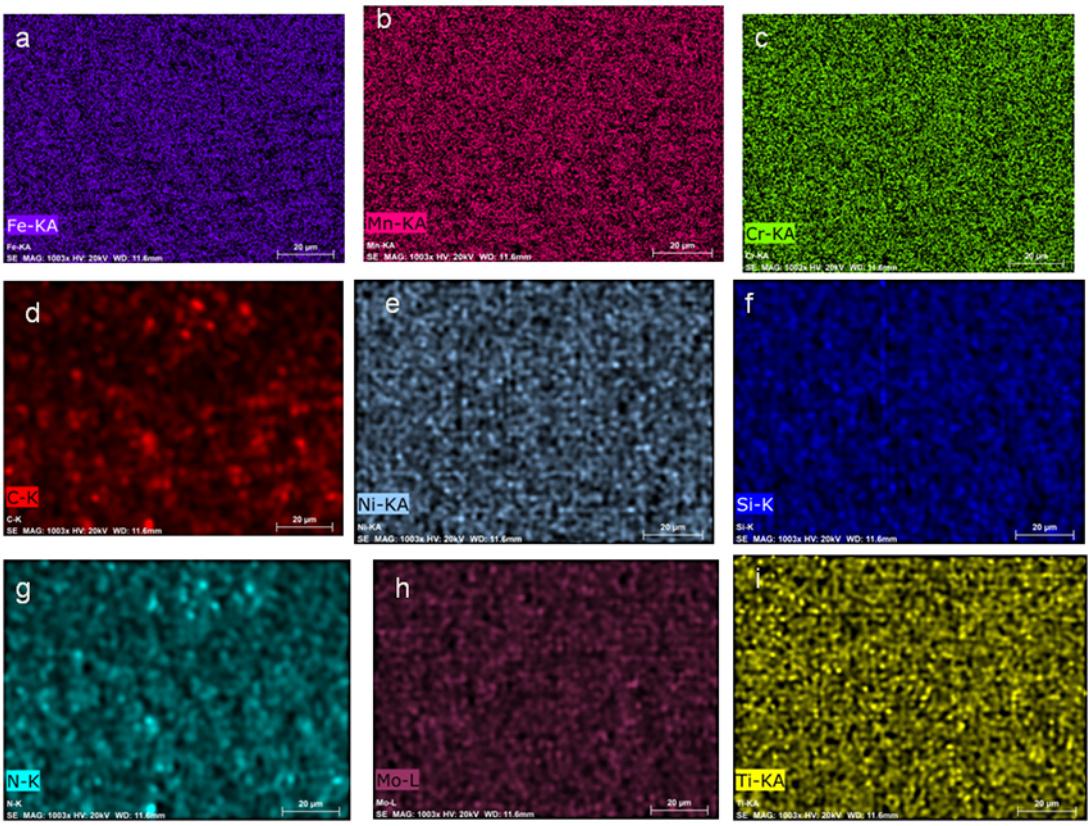

Figure 12. (a-i) EDS elements mapping of Experiment 3

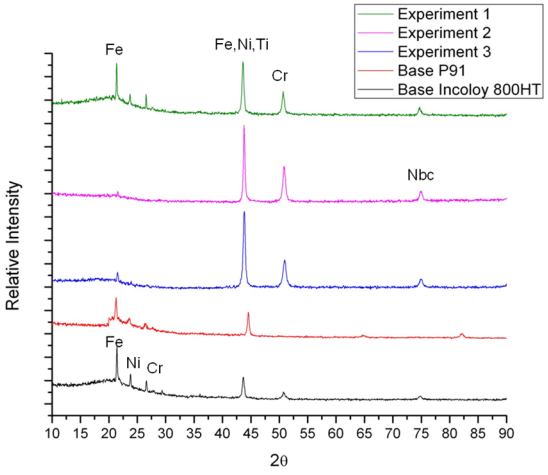

Figure 13. XRD analysis of base and weld materials

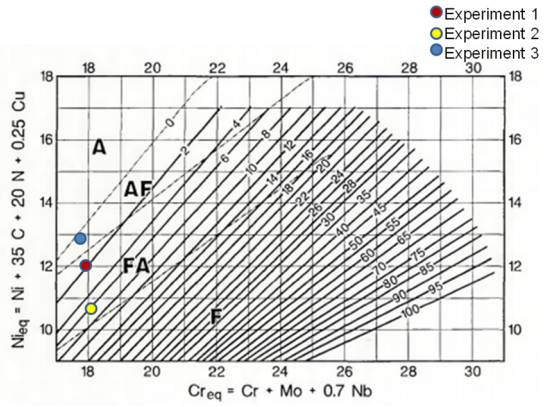

Figure 14. WRC-1992 diagram of experiment 1,2 and 3[30]

the Incoloy 800HT side the variations in the hardness were insignificant.

The hardness in the HAZ of P91 was highest compared to other regions because of the martensite phase formed due to rapid cooling rates in the laser welding. Microhardness values were in the range of 150HV-190$HV_{0.5}$ in the fusion zone (FZ), 403-432 $HV_{0.5}$ in the P91 HAZ, 170-188 $HV_{0.5}$ in Incoloy 800HT HAZ, 218-238 $HV_{0.5}$ in P91 base material and 150-170 $HV_{0.5}$ in the Incoloy 800 HT base metal. The microhardness value of the fusion zone comes between the microhardness values of the base metals. It is important to mention that steady increase in microhardness in the weld metal on crossing from the P91 to the Incoloy 800HT side till the weld center and gradually decrease in the microhardness can be seen. In Experiment 2, higher microhardness was obtained because of brittle intermetallic phases (FeNi, $TiFe_2$,TiNi,) and also due to the low ferrite content. Moreover, because of the carbon movement from the 9Cr-1Mo alloy

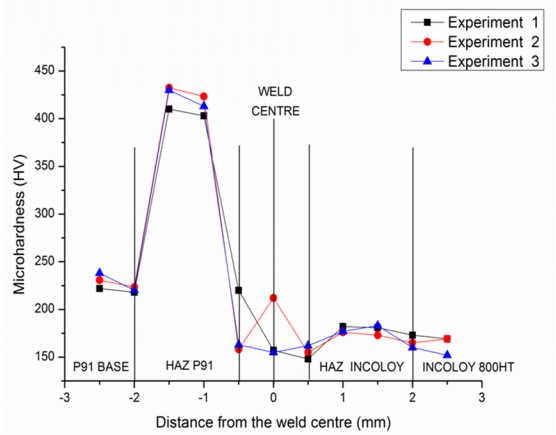

Figure 15. Microhardness graph of three different welds

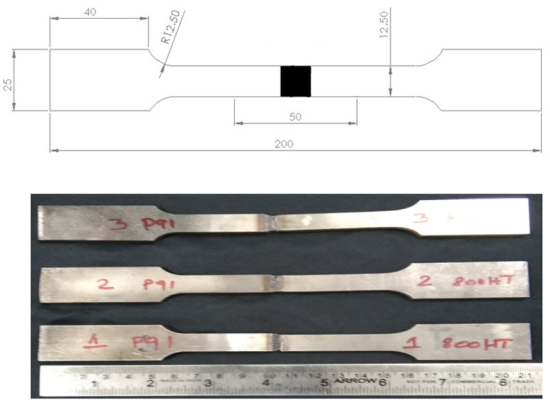

Figure 16. Tensile specimens ASTM E23 standard dimension and after testing

to the welds which in turn led to higher microhardness and obviously during tensile test, failure had occurred in the weld.

3.9 Tensile strength

To analyze the tensile strength and thereby to understand the failure spot and failure modes, transverse tensile tests were performed. The specimens before and after testing were shown in Fig 16. The samples of force and displacement curves are shown in Fig 17.

The tensile test results and the places of failure are presented in Table 4.

The failures in experiment 1 and 3 occurred in the HAZ of Incoloy 800HT side. This can be attributed to the brittle intermetallic phases in the HAZ of the Incoloy 800HT side and also due to the lower ferrite content in this region compared to other regions because of the martensite phase formed due to rapid cooling rates in the laser welding. It may be seen from all weld properties listed in Table 4 that experiment 3 has considerably higher strength than the other two welds. As welding involves high temperature, the diffusion of atoms is better stimulated especially in the cases involving dissimilar welding. A transition zone gets formed along the fusion boundary which is chemically diverse compared to both the base metals. The intermetallic compounds formed play an important role in affecting the tensile strength of the material. This may be attributed to the fact that strong nitride/carbide forming elements, like Nb, Ti, V, etc., have incomplete solubility in austenite and

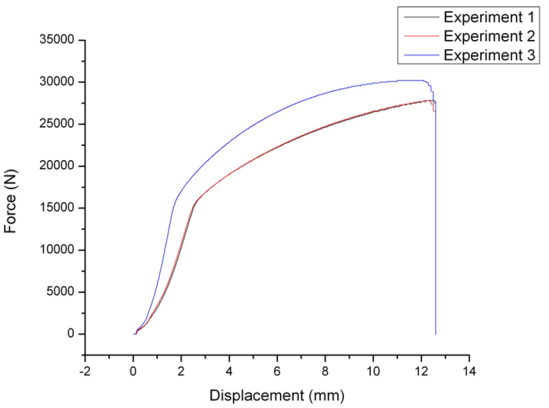

Figure 17. Force-displacement graph for three different welds

ferrite, and usually the precipitates act as fine dispersal of carbides, nitrides and carbonitride and contribute to tensile strength on account of precipitation hardening[27]. Generally, precipitation hardening tends to increase the tensile strength. This may be the reason that the Tensile strength of joint 3 gets increased when compared to the other two welds. Moreover, from the SEM images as shown in Fig 9(b) and (c) it is evident that Titanium carbide (TiC) and Titanium nitride (TiN) or carbonitride precipitates are formed at elevated temperature because of 0.06% carbon and 0.34% Titanium in Incoloy 800HT base metal. These observations are in line with Sayiram et al.[3]. This also confirms the above statement regarding the increase in the tensile strengths of

Table 4. Tensile test experimental results

Weld Trials	Ultimate Tensile Strength (MPa)	Elongation(%)	Places of Failure
P91 (RT)	635	21	-
Incoloy 800HT (RT)	530	60.157	-
Experiment 1	556	25.1	HAZ of Incoloy 800HT
Experiment 2	572	29.4	Weld
Experiment 3	604	38.6	HAZ of Incoloy800HT

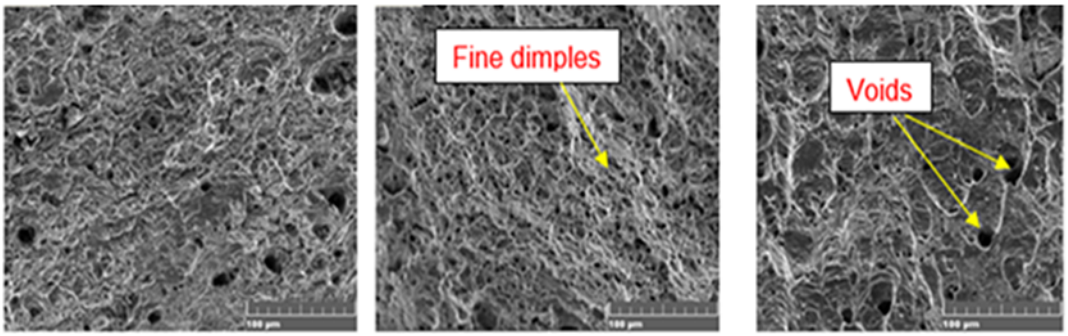

Figure 18. SEM fracture morphology at the fracture zone (a) experiment 1 (b) experiment2 (c) experiment 3

the joint 3 when compared with the tensile strength of other welds. The increase in the tensile strength may also be the result of the higher δ-ferrite content in Experiment 3 which drastically reduced the grain growth and it had deviated the crack propagation pathway. This is in line with the results obtained by Vashishtha et al[28]. It is understood that with increase in laser power, there was steady increase in the heat input to be weld which in turn increased the volume of the metal melted. A trend of increase in tensile strength was observed with increase in laser power.

3.10 Fractography of the tensile tested samples

Fractography was carried out using SEM to observe the fracture modes; it contained uniform dimples as shown in Fig 18(a-c) which revealed that the failure took place in a ductile mode.

Considering the differences in the place of failures, it seems that the cause for these variations was the differences in heat inputs, which led to dissimilar grain growth in the failure locations. The dimples form by a process called micro void coalescence, where voids nucleate and unite to develop the final fracture surface that is dimpled. The general process is one of pore development in a particle, subsequently either by localized shear band slip deformation in the inter void ligaments or void growth and linkage[29].

4. Conclusions

- Yb: YAG laser welding was successfully implemented for dissimilar welding of Incoloy800HT and P91 steel and the following observations were made from the experimental work,Macrostructures of welds revealed full penetration for all three experiments. There were no visible defects in experiment 2 and 3 weldments but weld obtained through experiment 1 had some porosities which was attributed to key hole instability.
- The solidification mode in the weld changed from cellular to fine equiaxed dendritic on moving from interface to center region. G/R ratio controlled the solidification mode while the product G * R controlled the size of the grains. Owing to higher G/R ratio in fusion line, solidification occurred in cellular mode and lower G/R ration in the weld center resulted in equiaxed dendrites.
- Through EDS elemental mapping, it was found that weld had both low density elements (Si, Ti, N, and C) and high density elements (Cr, Ni and Fe). Fe additon in the weld metal decreased the solubility of Nb in austenite.
- XRD analysis of dissimilar weld of Incoloy 800HT and P91 joints revealed the presence of brittle intermetallic compounds such as FeNi, $TiFe_2$,TiNi, and Nbc.
- Owing to the formation of martensite phase and rapid cooling, HAZ of P91 side had higher microhardness value than other regions.
- A trend of increase in tensile strength was observed with increase in laser power. Increase in the tensile strength was due to higher δ-ferrite content in experiment 3. The tensile failures in experiment 1 and 3 occurred in the HAZ of Incoloy 800HT side. This can be attributed to the brittle intermetallic phases in the HAZ of the Incoloy 800HT side and also due to the lower δ ferrite content in this region. Fractography analysis of all the welded samples revealed ductile mode of failure.

5. References

1. Sireesha M, Albert SK, Sundaresan S. Influence of high-temperature exposure on the microstructure and mechanical properties of dissimilar metal welds between modified 9Cr-1Mo steel and alloy 800. *Metallurgical and Materials Transactions A*. 2005;36(6):1495-1506.

2. Madhusudhan Reddy G, Mohandas T, Sambasiva Rao A, Satyanarayana VV. Influence of welding processes on microstructure and mechanical properties of dissimilar austenitic-ferritic

stainless steel welds. *Materials and Manufacturing Processes*. 2005;20(2):147-173. DOI: 10.1081/AMP-200041844

3. Sayiram G, Arivazhagan N. Microstructural characterization of dissimilar welds between Incoloy 800H and 321 Austenitic Stainless Steel. *Materials Characterization*. 2015;102:180-188. DOI: 10.1016/j.matchar.2015.03.006

4. Casalino G, Mortello M, Campanelli SL. Ytterbium fiber laser welding of Ti6Al4V alloy. *Journal of Manufacturing Processes*. 2015;20(Pt 1):250-256. DOI: 10.1016/j.jmapro.2015.07.003

5. Janaki Ram GD, Venugopal Reddy A, Prasad Rao K, Reddy GM, Sarin Sundar JK. Microstructure and tensile properties of Inconel 718 pulsed Nd-YAG laser welds. *Journal of Materials Processing Technology*. 2005;167(1):73-82. DOI: 10.1016/j.jmatprotec.2004.09.081

6. Shanmugarajan B, Sathiya P, Buvanashekaran G. Mechanical and metallurgical properties of autogenous laser welded P92 material. *Journal of Manufacturing Processes*. 2016;24:11-18. DOI: http://dx.doi.org/10.1016/j.jmapro.2016.07.003

7. Kou S. *Welding Metallurgy*. 2nd ed. Hoboken: John Wiley and Sons; 2003.

8. Das Neves MDM, Lotto A, Berretta JR, Rossi WD, Júnior NDV. Microstructure development in Nd: YAG laser welding of AISI 304 and Inconel 600. *Welding International*. 2010;24(10):739-748. DOI: 10.1080/09507110903568877

9. Silva CC, Miranda HC, de Sant'Ana HB, Farias JP. Austenitic and ferritic stainless steel dissimilar weld metal evaluation for the applications as-coating in the petroleum processing equipment. *Materials & Design*. 2013;47:1-8. DOI: 10.1016/j.matdes.2012.11.048

10. Kim JD, Kim CJ, Chung CM. Repair welding of etched tubular components of nuclear power plant by Nd: YAG laser. *Journal of Materials Processing Technology*. 2001;114(1):51-56. DOI: 10.1016/S0924-0136(01)00566-0

11. Han WJ, Byeon JG, Park KS. Welding characteristics of the Inconel plate using a pulsed Nd: YAG laser beam. *Journal of Materials Processing Technology*. 2001;113(1-3):234-237. DOI: 10.1016/S0924-0136(01)00718-X

12. Schneider A, Gumenyuk A, Lammers M, Malletschek A, Rethmeier M. Laser Beam Welding of Thick Titanium Sheets in the Field of Marine Technology. *Physics Procedia*. 2014;56:582-590. DOI: 10.1016/j.phpro.2014.08.046

13. Bhaduri AK, Srinivasan G, Gill TPS, Mannan SL. Effect of aging on the microstructure and tensile properties of alloy 800/9Cr-1Mo steel joint. *International Journal of Pressure Vessels and Piping*. 1995;61(1):25-33. DOI: 10.1016/0308-0161(94)P3696-J

14. Hauser D, Vanecho JE. Effects of ferrite content in austenitic stainless steel welds. *Welding Journal*. 1982;44:37s-44s.

15. Hull FC. Delta Ferrite and Martensite Formation in Stainless Steels. *Welding Journal*. 1973;52:193s-203s.

16. Kannan T DP, Sathiya P, Ramesh T. Experimental investigation and characterization of laser welded NiTinol shape memory alloys. *Journal of Manufacturing Processes*. 2017;25:253-261. DOI: 10.1016/j.jmapro.2016.12.006

17. Kuo TY, Lin YD. Effects of different Shielding Gases and Power Waveforms on Penetration Characteristics and Porosity Formation in Laser Welding of Inconel 690 Alloy. *Materials Transactions*. 2007;48(2):219-226. DOI: 10.2320/matertrans.48.219

18. Matsunawa A, Katayama S. Mechanism and prevention method of imperfection occurred in high power laser welding. In: *Proceedings of Joint Symposium between JWRI and TWI* ; 2001 Mar; Osaka, Japan.

19. Sireesha M, Shankar V, Albert SK, Sundaresan S. Microstructural features of dissimilar welds between 316LN austenitic stainless steel and alloy 800. *Materials Science and Engineering: A*. 2000;292(1):74-82. DOI: 10.1016/S0921-5093(00)00969-2

20. Dehmolaei R, Shamanian M, Kermanpur A. Microstructural characterization of dissimilar welds between alloy 800 and HP heat-resistant steel. *Materials Characterization*. 2008;59(10):1447-1454. DOI: 10.1016/j.matchar.2008.01.013

21. Yan J, Gao M, Zeng X. Study on microstructure and mechanical properties of 304 stainless steel joints by TIG, laser and laser-TIG hybrid welding. *Optics and Lasers in Engineering*. 2010;48(4):512-517. DOI: 10.1016/j.optlaseng.2009.08.009

22. Mortezaie A, Shamanian M. An assessment of microstructure, mechanical properties and corrosion resistance of dissimilar welds between Inconel 718 and 310S austenitic stainless steel. *International Journal of Pressure Vessels and Piping*. 2014;116:37-46. DOI: 10.1016/j.ijpvp.2014.01.002

23. Anawa EM, Olabi AG. Optimization of tensile strength of ferritic/austenitic laser-welded components. *Optics and Lasers in Engineering*. 2008;46(8):571-577. DOI: 10.1016/j.optlaseng.2008.04.014

24. Mirshekari GR, Saatchi A, Kermanpur A, Sadrnezhaad SK. Laser welding of NiTi shape memory alloy: Comparison of the similar and dissimilar joints to AISI 304 stainless steel. *Optics & Laser Technology*. 2013;54:151-158. DOI: 10.1016/j.optlastec.2013.05.014

25. Srinivasan PB, Satish Kumar MP. Microstructural and electrochemical characterization of a thin-section dissimilar stainless steel weld joint. *Materials Chemistry and Physics*. 2009;115(1):179-184. DOI: 10.1016/j.matchemphys.2008.11.044

26. David SA, Vitek JM. Correlation between solidification parameters and weld microstructures. *International Materials Reviews*. 1989;34(1):213-245. DOI: 10.1179/imr.1989.34.1.213

27. Brown IH. The role of microsegregation in centreline cold cracking of high strength low alloy steel weldments. *Scripta Materialia*. 2006;54(3):489-492. DOI: 10.1016/j.scriptamat.2005.09.047

28. Suder WJ, Williams SW. Investigation of the effects of basic laser material interaction parameters in laser welding. *Journal of Laser Applications*. 2012;24(3):032009. DOI: 10.2351/1.4728136

29. Becker WT, Lampman S. Fracture Appearance and Mechanisms of Deformation and Fracture. In: *ASM Handbook Volume 11, Failure Analysis and Prevention*. Materials Park: ASM International; 2002. p. 559-586.

30. Lippold JC, Kotecki DJ. *Welding Metallurgy and Weldability of Stainless Steels*. Hoboken: John Wiley and Sons; 2005.